MICROMECHANICAL MODELING OF THE NONLINEAR DEFORMATION OF LFTS UNDER CONSIDERATION OF THE EFFECTS OF INTERFACE DAMAGE

S. Fliegener[1], J. Hohe[1], B. Haspel[2] and K.A. Weidenmann[2]

[1]Business unit Component Safety and Lightweight Construction, Fraunhofer Institute for Mechanics of Materials IWM, Woehlerstrasse 11, D-79108 Freiburg, Germany
Email: sascha.fliegener@iwm.fraunhofer.de, web page: http://www.iwm.fraunhofer.de

[2]Institute for Applied Materials IAM-WK, Karlsruhe Institute of Technology KIT, Engelbert-Arnold-Strasse 4, D-76131 Karlsruhe, Germany
Email: kay.weidenmann@kit.edu, web page: http://www.iam.kit.edu/wk

Keywords: Micromechanical modeling, Interface damage, Long fiber reinforced thermoplastics

ABSTRACT

This work deals with the micromechanical finite element simulation of long fiber reinforced thermoplastics (LFT) under incorporation of the nonlinear deformation behavior of the matrix and the effects of fiber-matrix interface damage. The fiber-matrix debonding behavior is determined experimentally by single fiber push-out tests on thin slices, prepared from the cross section of the material. To extract the characteristics of the numerical interface model from the experimental curves, the push-out scenario is simulated and the properties of the interface are reversely determined in such a way that the experimental results of the push-out tests can be reproduced. The resulting values are then fed into a micromechanical finite element model of a LFT structure, described based on experimentally measured fiber orientation and length distributions. After implementation into the microstructural LFT model, the effects of interface damage can be captured in conjunction with the complex interactions on the material's microscale which arise from the locally varying fiber orientation, length and density. Thus, a mechanism-based interpretation of the stress-strain curve of macroscopic tensile tests on LFT specimens is enabled by comparison with the respective simulation results. The mechanisms considered are the plastic deformation of the matrix, the fiber-matrix interface debonding, the post-debonding friction and the brittle failure of the fibers. The potential increase in the material's strength and fracture strain by enhancement of its interface strength can finally be assessed by comparison of the simulations which account for a realistic and an imaginary, perfect interface.

1 INTRODUCTION

Long fiber reinforced thermoplastics (LFTs) are extremely promising with respect to their lightweight potential and their processability on large scale under application of the technologies of injection or compression molding. An inherent problem of most LFT material systems persists in the somewhat limited load transfer between the thermoplastic matrix and the fibers due to the absence of covalent bonds in contrast to thermoset-based systems. Various micromechanical testing methods are available to characterize the interface [1-6]. Furthermore, the effects of the interface on the composite's mechanical behavior and in particular the load transfer between the matrix and fibers have been investigated to a considerable extent by application of various modeling approaches, which were mainly developed for unidirectional fiber arrangements [7-10]. However, the equivalence of the mechanisms which govern the debonding behavior in the single fiber tests to those within a real composite material with a complex microstructure is not ensured [11]. To examine the transferability of the results from single-fiber push-out tests to a realistic microstructure, we study the effects of fiber-matrix debonding within a three dimensional model of the complex nonwoven structure of a LFT material [12]. For this purpose, single fiber push-out experiments on thin slices of the material were simulated and the parameters of the interface model describing the fiber-matrix debonding and the

post-debonding friction were inversely determined. The simulations of the LFT microstructure, which incorporate the interface properties from the push-out tests, are then compared to experiments on macroscopic specimens of the material to validate the modeling approach.

2 MATERIAL AND MICROSTRUCTURE

The investigated material (LFT PPGF30) consists of a polypropylene matrix (DOW® C711-70RNA) and glass fibers (TufRov® 4575) with 30 wt-% and 13.2 vol-%, respectively. It is produced by a direct compounding process, in which the fiber rovings are introduced directly into the mixing extruder [13]. The pre-product out of the direct compounding process, a mixture of the matrix polymer and the fibers with a rather weak orientation, is called LFT strand. A broad fiber length distribution results in which the maximum fiber length is determined by the thread of the screws of the mixing extruder. In detail, the maximum fiber length amounts to approx. 50 mm and a corresponding aspect ratio of approx. 3000, posing enormous challenges for the microstructural modeling due to the required data amount which is mandatory in order to incorporate the complete fiber length spectrum into the model. For mechanical characterization, plates of the LFT material with lateral dimensions of 400x400 mm² and a thickness of 3 mm were produced by compression molding. The LFT strand was placed asymmetrically in the mold, so that a distinct flow region develops anywhere outside the strand inlay position. Within the flow region, the degree of fiber orientation is significantly higher, governed by the local flow conditions and the shape of the mold. Dogbone shaped specimens with a reduced section of 70 x 10 mm² were cut out of the flow region of the plate under 0° and 90° orientation to the flow direction. CT scans were acquired on specimens of the same region of the plate in order to determine the fiber orientation distribution by image analysis of the CT data. Furthermore, a rectangular section of approx. 100x60 mm² was incinerated to extract the fiber length distribution. The resulting microstructural information in terms of fiber orientation and length distributions is specified in the work of Fliegener et al [12].

For the determination of the mechanical properties of the polypropylene matrix, dogbone shaped specimens were cut out of plates produced by injection compression molding, containing the same additives, stabilizers and coupling agents which were used to produce the LFT material, so that the properties of the matrix substance specimens are similar to the matrix material within the composite.

3 EXPERIMENTAL METHODS

3.1 Single fiber push-out

To characterize the fiber-matrix debonding behavior, single fiber push-out experiments were performed on a 85 µm thin slice of the LFT material. The slice with lateral dimensions of approx. 20x3 mm² was prepared from the cross section of the specimen plate and thus contains the majority of the fibers parallel to its thickness direction (approx. 85 µm). The slice was polished with diamond suspension of subsequently refined granulation to obtain a sufficiently smooth surface. The slice was then placed on a perforated plate with a hole diameter of approx. 60 µm and a grid distance of approx. 200 µm. Fibers located within a hole of the perforated plate were selected manually for indentation. The indents were performed with a modified hardness testing machine (Zwick ZHU 0.2), equipped with a flat punch indenter of approx. 5 µm tip diameter, which is sufficiently small compared to the nominal fiber diameter of 17 µm. A maximum indentation depth of 6 - 8 µm, measured after the initial contact of indenter and fiber, was reached in displacement-controlled mode at a rate of approx. 3 µm / min. The experimental setup is shown in Fig. 1.

3.2 Tensile tests on matrix and LFT specimens

To determine the mechanical properties of the polypropylene matrix and the LFT material, quasi-static tensile tests were carried out. The tests were performed at a nominal strain rate of $7 \cdot 10^{-4}$ 1/s which was chosen equally for the matrix and the LFT specimens. In case of the LFT material, specimens under 0° and 90° to the flow direction were tested. The strain was acquired by a clip-on extensometer with a reference length of 50 mm.

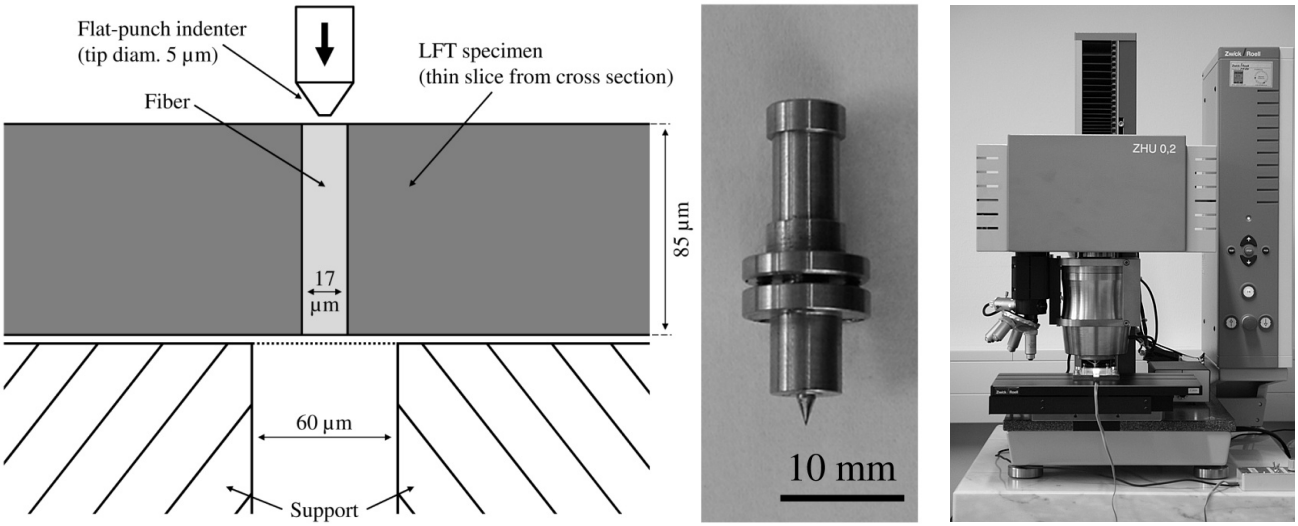

Figure 1: Experimental setup of the single fiber push-out tests: Loading scenario with the thin slice (LFT specimen) bearing on a perforated plate with 60 µm hole diameter (left), flat-punch indenter (approx. 5 µm tip diameter, middle) and modified Zwick ZHU 0.2 hardness tester (right).

4 MODELING TECHNIQUES

4.1 Multidirectional LFT structure

The modeling of a multidirectional LFT structure in the form of a representative volume element (RVE) has been described by Fliegener et al. [12]. In the first step, a stack of straight fibers was generated under compliance of the experimentally measured, planar fiber orientation distribution. The stack of fibers was then compressed to the desired value of fiber volume fraction (13.2 vol-%). A contact formulation with a non-zero offset was activated for the explicit finite element simulation of fiber compression, resulting in a minimum distance between the fibers to avoid any overlapping and interpenetration which would be unrealistic. In the last step of the structure generation procedure, the remaining gaps between the fibers and the RVE boundary are filled with a tetrahedral mesh, representing the matrix. The structure investigated in this work is similar to the RVE of PPGF30 (13.2 vol-%) described in [12] with the same microstructural characteristics, but features additional cohesive zone elements between the fibers and the matrix to model the debonding behavior (Fig. 2).

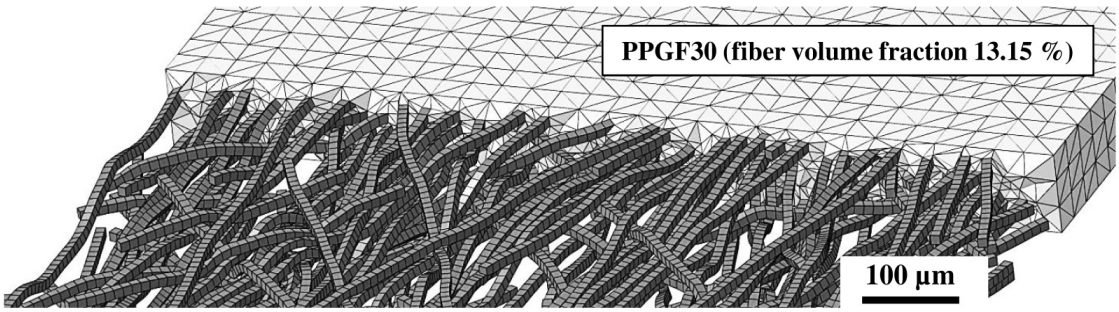

Figure 2: Mesh details of the investigated LFT structure: A close-up of the RVE with lateral dimensions of 50 x 1.5 x 0.134 mm³ is shown with a part of the matrix mesh removed. The structure has been generated under incorporation of the experimentally measured fiber orientation and length distributions as well as the value of nominal fiber volume fraction [12].

4.2 Single fiber push-out

The purpose of the modeling of the push-out scenario is the inverse determination of the parameters of the traction-separation law which is assigned to the cohesive zone elements between the fibers and the matrix and needs to be interpreted as a pragmatic approach to mimic the behavior of the interface with no profound physical background. Furthermore, the element size of the push-out model must be chosen equally to that of the multidirectional LFT structure in order to ensure the transferability of the results, since stress singularities (e.g. at the fiber ends) would be reproduced differently if the element size would vary. Due to the extreme aspect ratio of the investigated material of 3000 and the resulting enormous size of the multidirectional models, the fibers need to be depicted by a single hexahedral element over their cross section for reasons of computational efficiency. Thus, the same coarse mesh must be applied for the modeling of the push-out scenario. Since the load direction is parallel to the fiber axis, the edge effects because of the coarse discretization can be expected as weak. Nevertheless, it needs to be emphasized that the model represents a pragmatic, engineering approach to incorporate the interface properties from the single-fiber tests in the large multidirectional structures.

The finite element mesh of the fiber push-out scenario is shown in Fig. 3. A circular section of the matrix material was modeled, surrounding the fiber in its center. In analogy to the experiments, where the specimen bears on a perforated plate, the nodes outside the inner circular section of 60 µm (representing the hole diameter of the plate) are constrained in their degree of freedom in fiber push-out direction. Cohesive zone elements were added in between the fiber and the matrix, but are not visible in the figure due to their very small thickness of $1 \cdot 10^{-5}$ mm. Both the fibers and the matrix were modeled linear elastic and isotropic with their elastic constants set to the values specified in the manufacturer's data sheet (E_m = 1250 MPa, ν_m = 0.35, E_f = 72 000 MPa, ν_f = 0.22). The parameters of the traction-separation law, which was assigned to the cohesive elements to represent the debonding behavior, were determined inversely so that the force-displacement curves of the push-out simulations were similar to the experimental results. In a second study, the effects of post-debonding friction were considered by additional activation of a general contact formulation (*Abaqus Explicit*) with a non-zero coefficient of friction.

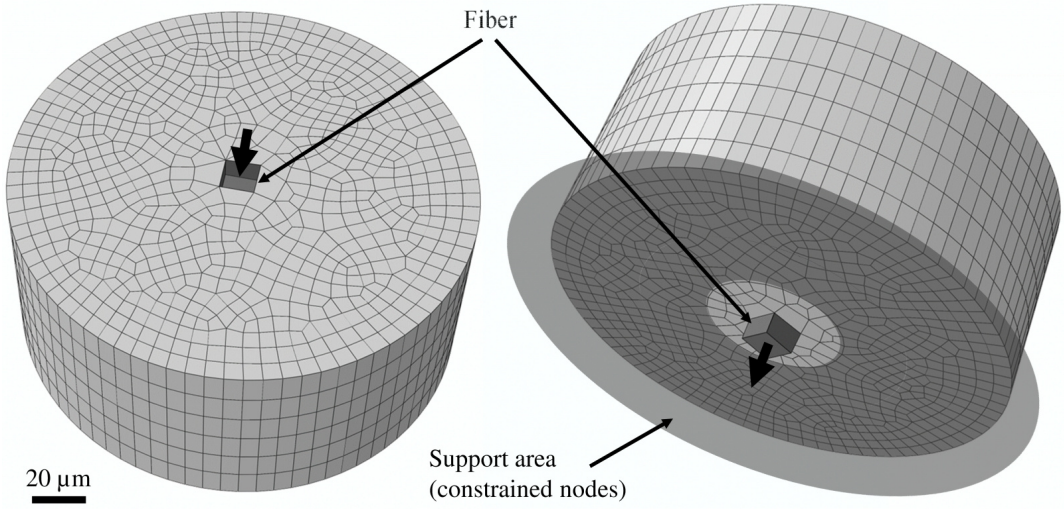

Figure 3: Finite element mesh of the fiber push-out scenario for the inverse determination of the fiber matrix interface properties. The bold arrows highlight the push-out direction (left: top view, right: bottom view).

A traction-separation law according to Dugdale [14] and Barenblatt [15] was chosen to describe the debonding behavior of the interface. A virtual elastic part of deformation of the cohesive elements is necessary for numerical reasons, followed by the actual description of the debonding in terms of a

damage evolution. The elastic part of the model does not feature a coupling between the normal (*n*) and the shear components (*s,t*) of the traction $\underline{t}$ and nominal strain $\underline{\varepsilon}$. Thus, the stiffness matrix $\underline{K}$ has only diagonal components:

$$\begin{pmatrix} t_n \\ t_s \\ t_t \end{pmatrix} = \begin{bmatrix} K_n & & \\ & K_s & \\ & & K_t \end{bmatrix} \begin{pmatrix} \varepsilon_n \\ \varepsilon_s \\ \varepsilon_t \end{pmatrix} \tag{1}$$

where $\underline{\varepsilon} = \underline{\delta} / h$ is the nominal strain (the separation vector $\underline{\delta}$ divided by the nominal thickness of the interface *h*). The components of the stiffness matrix were set equal to $K = K_n = K_s = K_t$ since they have no physical meaning and represent a numerical aid.

A quadratic criterion for the nominal strain defines the threshold of damage initiation:

$$\left(\frac{\langle \varepsilon_n \rangle}{\varepsilon_n^0}\right)^2 + \left(\frac{\varepsilon_s}{\varepsilon_s^0}\right)^2 + \left(\frac{\varepsilon_t}{\varepsilon_t^0}\right)^2 = 1 \tag{2}$$

with the superscript *0* denoting the respective threshold for each component and the < >-operator affecting that no compressive normal stresses can cause any damage. Again, the components of $\underline{\varepsilon}^0$ were set equal to $\varepsilon^0 = \varepsilon^0_n = \varepsilon^0_s = \varepsilon^0_t$. After the criterion for damage initiation is met, the traction stress of the respective element is degraded by a scalar damage variable *D*, in which a value of 0 represents an undamaged state and a value of 1 corresponds to a completely damaged element:

$$t_{n,s,t} = (1-D) t^*_{n,s,t} \tag{3}$$

where $t^*_{n,s,t}$ is the traction stress of the undamaged element. During the evolution of damage, the damage variable *D* increases linearly until the effective maximum displacement δ^* is reached:

$$\delta^* = \sqrt{\langle \delta_n \rangle^2 + \delta_s^2 + \delta_t^2} \tag{4}$$

5 RESULTS

5.1 Single fiber push-out

The force-displacement curves of both simulation variants (debonding only / debonding and friction) are depicted together with the corresponding experiments in Fig. 4. As it can be seen in the figure, the behavior up to the force peak is similar for both variants, whereas the force plateau above a displacement of approx. 2 µm can exclusively be reproduced by the variant under activation of the contact formulation with incorporation of friction. Because the cohesive elements fail successively starting at the fiber ends, the activation of friction also influences the shape of the curves before the load peak (if an element is deleted, a part of its initial load carrying capacity is still retained by friction). Consequently, the debonding parameters (failure displacement of the traction-separation law) need to be chosen differently for the variant which considers friction. The parameters of both simulation variants are specified in Table 1.

It is remarkable that the force peak of the experimental curves, which feature only a moderate degree of scatter, can be captured quite accurately by both simulation variants, whereas the initial stiffness of the experimental curves is overestimated to a certain degree by the simulations. Likely reasons are the presence of a setting behavior of the flat-punch indenter when the initial contact to the fiber is established and an angular deviation between the fiber orientation and the push-out direction due to the varying orientation of the fibers inside the sample. However, numerical studies of an imperfect fiber alignment during push-out revealed a rather weak extent of this effect [16]. Furthermore, the presence of neighboring fibers does not extensively distort the results, as an exemplary evaluation under application of the same methods shows [17].

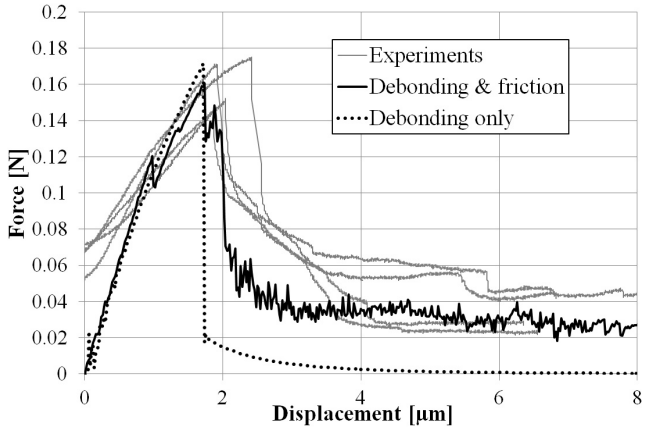

Figure 4: Force-displacement curves of single fiber push-out experiments and corresponding simulation results under activation of debonding only / debonding and post-debonding friction.

Another possible reason for the overestimated initial stiffness lies in the relatively coarse mesh to describe the push-out scenario (Fig. 3) which was chosen similar to the mesh of the RVEs (Fig. 2, in this case, the coarse mesh is mandatory for computational performance). Thus, the elastic deflection of the part of the matrix between the fiber and the support area might be underestimated by the simulations.

Parameter	**Unit**	**Debonding only**	**Debonding and friction**
Nominal thickness of cohesive section	[mm]	$1 \cdot 10^{-5}$	$1 \cdot 10^{-5}$
Mass density	[t/mm^3]	$2 \cdot 10^{-9}$	$2 \cdot 10^{-9}$
Stiffness of elastic traction (K)	[N/mm]	10	10
Displacement of damage initiation	[mm]	0.005	0.005
Displacement of damage evolution (corresponding stiffness degradation of 1)	[mm]	0.00025	0.00015
Coefficient of friction		-	2
Global surface thickness assignment (general contact formulation)	[mm]	-	$1 \cdot 10^{-5}$

Table 1: Parameters of the traction-separation model to describe the fiber-matrix debonding and the optional contact formulation to model the effects of post-debonding friction.

5.2 Matrix plasticity

The elasto-plastic deformation behavior of the polypropylene matrix was determined by quasi-static tensile tests on matrix substance specimens, which were performed at the same nominal strain rate as the validation experiments on LFT specimens ($7 \cdot 10^{-4}$ 1/s). For numerical representation, a classical von Mises plasticity law (available in *Abaqus* under the keyword **PLASTIC*) was chosen. For stresses above the equivalent yield stress

$$\sigma_Y = \sqrt{3/2 \; \sigma'_{ij} \, \sigma'_{ij}} \tag{5}$$

the equivalent plastic strain ε_p can be obtained by integration of the equivalent plastic strain rate $\dot{\varepsilon}_p$ over the time increment dt:

$$\varepsilon_p = \int_0^t \dot{\varepsilon}_p \, dt \tag{6}$$

where the equivalent plastic strain rate $\dot{\varepsilon}_p$ is defined as

$$\dot{\varepsilon}_p = \sqrt{2/3\ \dot{\varepsilon}_{ij}^p\ \dot{\varepsilon}_{ij}^p} \tag{7}$$

The evolution of the isotropic hardening, which was specified in terms of tabular values of yield stress σ_Y and corresponding equivalent plastic strain ε_p, is shown in Fig. 5 in together with the response of a characteristic matrix specimen. The values are specified in Table 2. The apparent softening of the experimental curve above a total strain of approx. 0.04 was not considered since engineering measures of stress and strain were used and thus, the decrease of stress is likely caused by specimen necking, which is not captured here. Furthermore, no strain-rate dependency is considered by the model. A sensitivity analysis showed that the chosen values of strain rate within the quasi-static range are sufficiently low, so that the rate effects of the material are not significant.

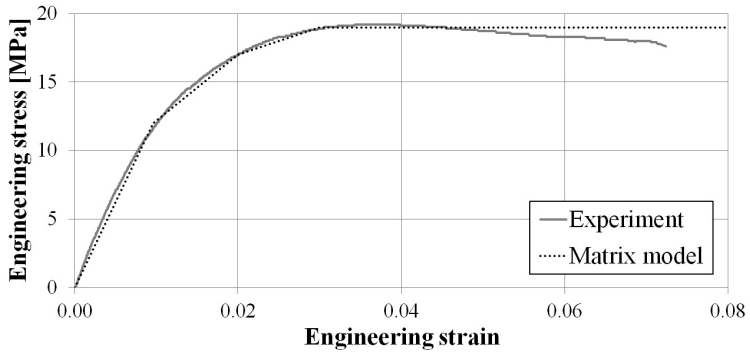

Figure 5: Calibration of the von Mises plasticity model with a quasi static tensile test on a matrix substance specimen (nominal strain rate $7 \cdot 10^{-4}$ 1/s).

In detail, experiments under a variation of the strain rate between $7 \cdot 10^{-5}$ 1/s $\leq \dot{\varepsilon} \leq 7 \cdot 10^{-3}$ 1/s showed a very weak deviation in their hardening behavior. Thus, the negligence of a rate dependency by the matrix model seems to be acceptable for the investigated quasi-static regime. It needs to be emphasized that such negligence is not justified if the range of validity of the modeling should be extended to higher strain rates, such as the load case of crash.

Total strain ε_{tot} [-]	**Plastic strain ε_p [-]**	**Yield stress σ_Y [MPa]**
0.0096	0	12
0.02	0.0104	17
0.03	0.0204	19

Table 2: Parameters of the elasto-plastic material model to describe the deformation behavior of the matrix. A classical von Mises plasticity law with isotropic hardening was chosen. The elastic properties are E_m = 1250 MPa, ν_m = 0.35.

5.3 Multidirectional LFT structure

To investigate the effects of different deformation and damage mechanisms on the stress-strain curve of LFT, several variants of the RVE (Fig. 2) were simulated and compared to corresponding experiments on LFT specimens under 0° and 90° load direction relative to the material's flow direction. The original RVE as described in [12] features a high degree of elongation: the dimension parallel to the flow direction was chosen to 50 mm to include the complete fiber length spectrum. To limit the model size to a reasonable value of 10^6 elements (the maximum which was computable with

the available resources), it was necessary to crop the RVE in transverse direction to a much smaller value of 1.5 mm. Consequently, the RVE is only suitable to investigate the behavior in flow direction (Fig. 6, left). A second RVE with a base section of 5 x 5 mm² was therefore analyzed to predict the transverse behavior (Fig. 6, right), since the edge length of 5 mm still captures the most important part of the fiber length distribution and because of less fibers being aligned in transverse direction, the fiber length distribution has no such drastic effect as in flow direction. The shortened RVE dimension of 5 mm is therefore acceptable in this case, in contrast to 0° load direction, where it is mandatory to include the full fiber length spectrum up to 50 mm.

Fig. 6 shows the response of the simulation variants accounting for matrix plasticity only (representing an imaginary, perfect fiber-matrix interface, denoted as *'No debonding'*), matrix plasticity and fiber-matrix debonding (neglecting the effects of friction during fiber pullout, labeled *'Debonding only'*) as well as matrix plasticity, fiber-matrix debonding and post-debonding friction (*'Debonding and friction'*). The simulations were aborted when first fiber failure occurred, corresponding to the end of the stress-strain curves. A brittle fracture criterion was always activated, with a fiber failure stress of 2500 MPa, which has been chosen from the middle of the range of 1800-3500 MPa which is referred in the literature [18-20]. No damage of the matrix can currently be described since this would require a highly uniform and refined matrix mesh to accurately predict the energy dissipation during the damage evolution phase. This was not possible within the available computational resources (to limit the number of elements to 10^6 it was necessary to allow a variation in element size as it can be observed in Fig. 2). Furthermore, a significant amount of mass scaling of the explicit finite element simulations (*Abaqus Explicit*) was necessary to allow the computation of the models in a reasonable time, resulting in a significant degree of oscillation of the numerical stress-strain curves. A sensitivity analysis was carried out with varying values of mass scaling with the result that the observed oscillation of the curves can be considered as a cosmetic effect and does not distort the results in an invalid way.

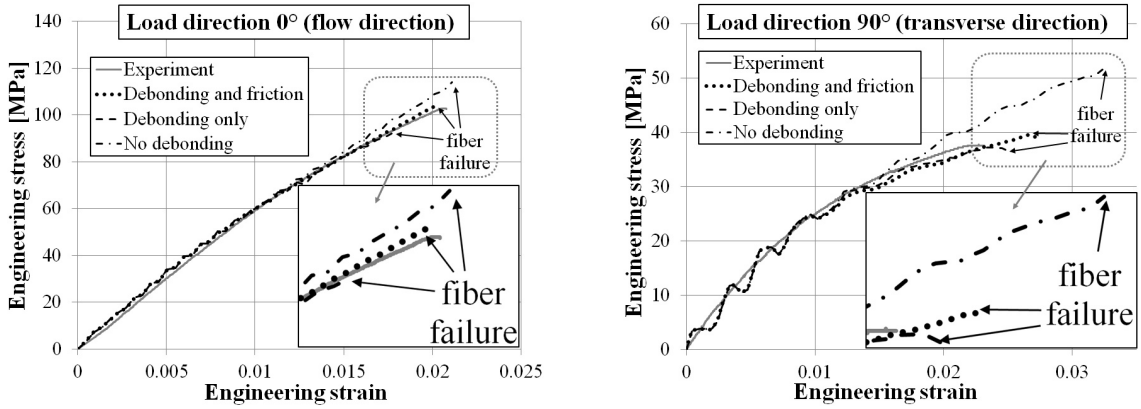

Figure 6: Results of the microstructural simulations of the LFT material: The stress-strain curves of the simulations are compared to a validation experiment of the LFT material for a load direction of 0° (left) and 90° (right). The simulations were performed under activation of different deformation and damage mechanisms which are further described in the text.

In 0° load direction (Fig. 6, left), the three simulation variants deviate only to a minor degree and are all in good agreement to the experimental result. Since the fibers are sufficiently long, the effects of debonding are relatively weak and the load transfer is not diminished drastically, even close to the point of fracture of the composite. Furthermore, the difference between the simulation results is small compared to the degree of experimental scatter (for the sake of clarity, only a single characteristic experiment is depicted). Thus, the interpretation of the different mechanisms, as discussed in the following, is restricted to the numerical studies with the aim to gain a principle understanding of the deformation and damage behavior of the complex fiber structures. Nevertheless, it is remarkable that the flattening of the experimental curve toward the point of failure is not captured by the simulation

which considers a perfect interface (*'No debonding'*) and that the variant which does not incorporate the effects of friction (*'Debonding only'*) fails significantly earlier than the remaining variant (*'Debonding and friction'*). A significant part of the load transfer is therefore apparently retained by post-debonding friction and the failure of short fibers in pullout mode (the circumferential area of a short fiber is too small to build up the critical tensile stress, thus it fails by pullout rather than normal fracture) is delayed to a higher composite strain. In contrast, the initial load carrying capacity of the debonded, short fibers is completely lost for the variant considering debonding only, and therefore, this part of the load needs to be transferred to the longer fibers, which consequently reach their value of normal failure stress at a lower effective composite strain compared to the variants under consideration of friction and the perfect interface.

In 90° load direction (Fig. 6, right), the effects of the different mechanisms are significantly more pronounced. It is remarkable that here, the variants accounting for debonding only / debonding and friction almost coincide. Apparently, the load transfer by friction has no significant effect since the majority of fibers is loaded transverse to its interface and thus fails in the same way of pure interface debonding, independent of friction. The difference in effective composite fracture stress and strain to the variant with a perfect interface is therefore quite considerable and represents the potential increase in the effective properties of the LFT material, if its interface strength could be enhanced. This is illustrated in Fig. 7. Furthermore, in agreement to the 0° results, the flattening of the stress-strain curve during its last part can exclusively be captured if fiber-matrix debonding is activated.

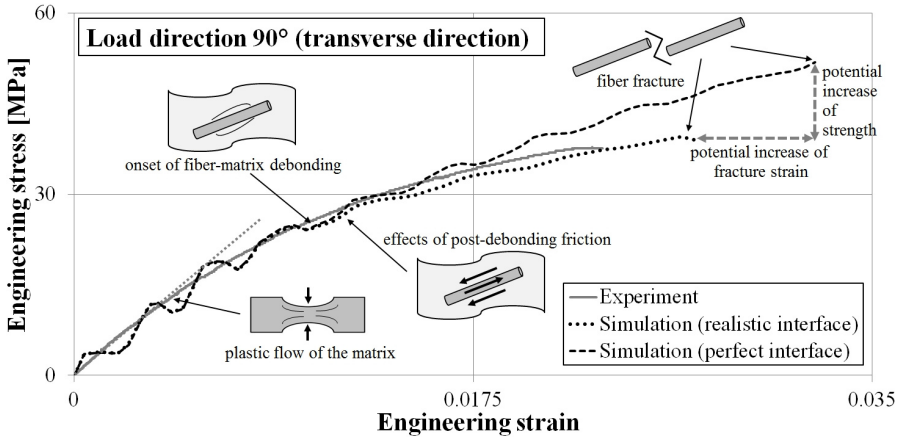

Figure 7: Interpretation of the stress-strain curves of LFT simulations and an experiment for 90° load direction. The difference between the simulation which accounts for interface damage and the one which considers a perfect interface represents the potential increase in the effective composite properties which can be employed by an enhanced fiber-matrix interface strength.

The contour plots at the time of failure are shown in Fig. 8. The left part of the figure visualizes the equivalent von Mises stress within the fiber elements of the simulation which incorporates the effects of debonding and post-debonding friction in 0° load direction. The amount of long fibers (up to the maximum fiber length of 50 mm of the implemented fiber length distribution) aligned in load direction is sufficiently high, so that the normal fracture stress builds up and the structure fails at its weakest cross section by normal fiber fracture. The maximum von Mises stress observed is slightly larger than the specified failure stress of 2500 MPa since it was necessary to consider a non-zero, but very small amount of damage evolution energy for numerical reasons.

In contrast, the right part of Fig. 8 shows a different structure with a significantly decreased and uniform fiber length of 1.2 mm which was simulated with activation of debonding only (no friction). Thus, the rather short fibers all fail catastrophically by pullout (pure interface damage), since their circumferential area is too small to build up the critical fracture stress within the fibers in analogy to

the model of Kelly and Tyson [7], represented numerically by localization of the scalar degradation factor D (Eq. 3) within the cohesive zone elements of the weakest cross section of the RVE.

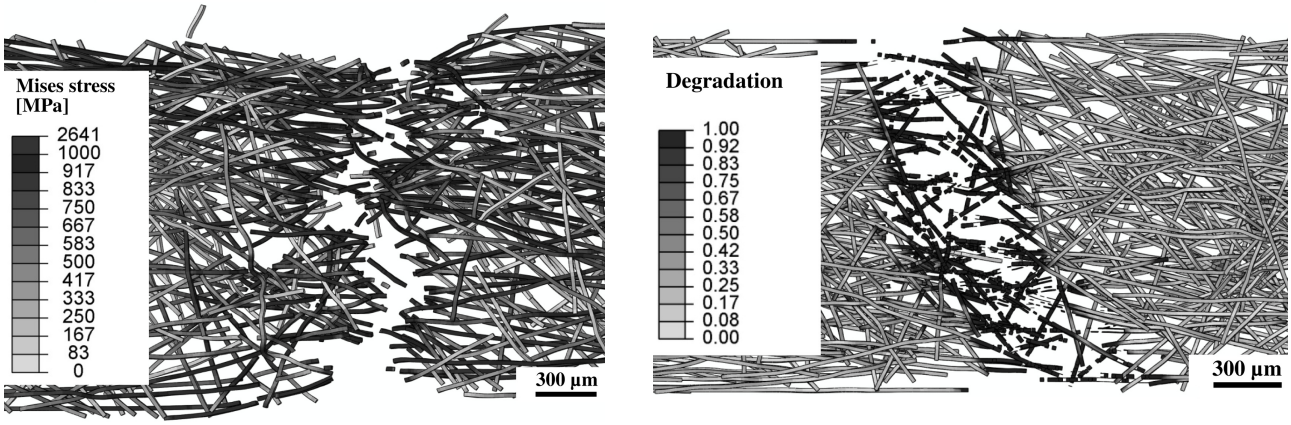

Figure 8: Damage localization within the fiber elements of a structure with implemented fiber length distribution (maximum fiber length of 50 mm) which was simulated under activation of debonding and post-debonding friction (left, the legend refers to the von Mises stress). The structure fails by normal fiber fracture at its weakest cross section. A different structure with a uniform fiber length of 1.2 mm was analyzed with activation of debonding only (no friction) and shows a localization of damage within the cohesive elements (right, the legend refers to the scalar damage degradation factor). Here, all fibers fail in pullout mode, since the normal failure stress cannot be built up within the fibers due to their short length. The matrix elements have been removed for both figures.

6 CONCLUSIONS

It is remarkable that in our studies, the incorporation of the interface properties (determined reversely by the simulation of single fiber push-out) into the multidirectional LFT structures with a complex microstructure yields very reasonable results. Thus, it seems in general to be feasible to combine different mechanisms, which were measured with independent experiments on different scales (e.g. single fiber tests on the micro level and macroscopic tensile tests on representative LFT samples) to a holistic microstructural model. In particular, the flattening of the experimental stress-strain curves of both load directions can exclusively be captured by the simulations accounting for the effects of fiber-matrix debonding. The point of the onset of interface damage can therefore be identified in the macroscopic response of the LFT specimens.

Furthermore, the potential increase in the effective material properties by enhancement of its interface strength can be evaluated based on the difference of the stress-strain curves of the simulations which consider a realistic and a perfect interface. This potential seems to be particularly large in transverse load direction, where the majority of fibers is loaded normal to its interface. In this context, it needs to be mentioned that the interface properties were calibrated with push-out tests, where a shear loading of the interface is dominant. Additional information for the calibration of the interface model in normal direction would be necessary to ensure the validity of the results. For example, such information could be provided by single fiber Broutman tests [2], in which the interface is predominantly loaded in normal direction. Furthermore, loading-unloading cycles during the macroscopic tensile tests on LFT specimens would represent an additional validation of the model, since the effects of interface damage would affect the slope of the re-loading path to decrease compared to the initial stiffness of the stress-strain curves.

The presented, mechanism-based modeling can be helpful to understand the load transfer within the complex fiber structure of LFTs with a spatially varying fiber orientation and length distribution. The findings agree to the fundamental views of Kelly and Tyson [7], where fibers which are too short to build up their critical tensile stress by the load transfer over their interface region are pulled out,

whereas sufficiently long fibers fail by normal fracture. The interaction of the different microstructural mechanisms under conditions which are difficult to achieve by experiments, such as multiaxial load states, can be visualized by models like ours. In the end, the model has considerable potential to support the development of advanced effective material laws which are suitable for the simulation of LFT parts or components under incorporation of the investigated, microscopic mechanisms.

ACKNOWLEDGEMENTS

Financial support of the *KITe hyLITE* innovation cluster and the Fraunhofer internal project *MEF LFT-Baukasten (826243)* is gratefully acknowledged. The authors would like to thank B. Hangs at Fraunhofer ICT for providing the material and R. Schlimper at Fraunhofer IWM for CT analysis.

REFERENCES

[1] S. Zhandarov, E. Mäder, Characterization of fiber/matrix interface strength: applicability of different tests, approaches and parameters, *Composites Science and Technology*, **65**, 2005, pp. 149-160.

[2] C. Ageorges, K. Friedrich, T. Schüller, B. Lauke, Single-fibre Broutman test: fibre–matrix interface transverse debonding, *Composites Part A*, **30**, 1999, pp. 1423-1434.

[3] M. N. Kallas, D. A. Koss, H. T. Hahn and J. R. Hellmann, Interfacial stress state present in a "thin-slice" fibre push-out test, *Journal of Materials Science*, **27**, 1992, pp. 3821-3826.

[4] G. P. Tandon, N. J. Pagano, Micromechanical analysis of the fiber push-out and re-push test, *Composites Science and Technology*, **58**, 1998, pp. 1709-1725.

[5] R. J. Kerans, T. A. Parthasarathy, Theoretical Analysis of the Fiber Pullout and Pushout Tests, *J. Am. Ceram. Soc.*, **74**, 1991, pp. 1585-1596.

[6] J. A. Nairn, Analytical fracture mechanics analysis of the pull-out test including the effects of friction and thermal stresses, *Advanced Composites Letters*, **9**, 2000, pp. 373-383.

[7] A. Kelly, W. R. Tyson, Tensile properties of fibre-reinforced metals: Copper/Tungsten and Copper/Modybdenum, *J. Mech. Phys. Solids*, **13**, 1965, pp. 329-350.

[8] H. L. Cox, The elasticity and strength of paper and other fibrous materials, *British Journal of Applied Physics*, **3**, 1952, pp. 72-79.

[9] J. A. Nairn, On the use of shear-lag methods for analysis of stress transfer in unidirectional composites, *Mechanics of Materials*, **26**, 1997, pp. 63-80.

[10] Z. Xia, T. Okabe, W. A. Curtin, Shear-lag versus finite element models for stress transfer in fiber-reinforced composites, *Composites Science and Technology*, **62**, 2002, pp. 1141-1149.

[11] M. R. Piggott, Why interface testing by single-fibre methods can be misleading, *Composite Science and Technology*, **57**, 1997, pp. 965-974.

[12] S. Fliegener, M. Luke, P. Gumbsch, 3D microstructure modeling of long fiber reinforced thermoplastics, *Composites Science and Technology*, **104,** 2014, pp. 136-145.

[13] F. Henning, H. Ernst, R. Brüssel, O. Geiger, W. Krause, LFTs for automotive applications, *Reinforced Plastics,* **49**, 2005, pp. 24-33.

[14] D. S. Dugdale, Yielding of steel sheets containing slits, *Journal of the Mechanics and Physics of Solids*, **8**, 1960, pp. 100-104.

[15] G. I. Barenblatt, The mathematical theory of equilibrium cracks in brittle fracture, *Advances in applied mechanics*, **7**, 1962, pp. 55-129.

[16] B. Brylka, F. Fritzen, T. Böhlke, K. A. Weidenmann, Influence of micro-structure on fibre push-out tests, *Proc. Appl. Math. Mech.*, **11**, 2011, pp. 141-142.

[17] B. Brylka, F. Fritzen, T. Böhlke, K. A. Weidenmann, Study of Experimental Methods for Interface Problems Based on Virtual Testing, *Proc. Appl. Math. Mech.*, **10**, 2010, pp. 109-110.

[18] F. M. Zhao, T. Okabe, N. Takeda, The estimation of statistical fiber strength by fragmentation tests of single-fiber composites, *Composites Science and Technology*, **60**, 2000, pp. 1965-1974.

[19] J. Andersons, R. Joe, M. Hojo, S. Ochiai, Glass fibre strength distribution determined by common experimental methods. *Composites Science and Technology*, **62**, 2002, pp. 131-145.

[20] J. L. Thomason, L. Yang, R. Meier, The properties of glass fibres after conditioning at composite recycling temperatures. *Composites: Part A*, **61**, 2014, pp. 201-208.